Accepted Manuscript

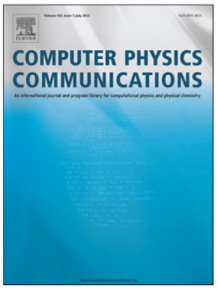

Non-linear wave generation and absorption using open boundaries within DualSPHysics

Tim Verbrugghe, J.M. Domínguez, Corrado Altomare,
Angelantonio Tafuni, Renato Vacondio, Peter Troch,
Andreas Kortenhaus

PII: S0010-4655(19)30046-3
DOI: https://doi.org/10.1016/j.cpc.2019.02.003
Reference: COMPHY 6732

To appear in: *Computer Physics Communications*

Received date : 28 July 2018
Revised date : 20 December 2018
Accepted date : 4 February 2019

Please cite this article as: T. Verbrugghe, J.M. Domínguez, C. Altomare et al., Non-linear wave generation and absorption using open boundaries within DualSPHysics, *Computer Physics Communications* (2019), https://doi.org/10.1016/j.cpc.2019.02.003

Non-linear wave generation and absorption using open boundaries within DualSPHysics

Tim Verbrugghe [1*], J.M. Domínguez [2], Corrado Altomare[1,3], Angelantonio Tafuni[4], Renato Vacondio[5] , Peter Troch [1], Andreas Kortenhaus[1*]

[1] *Department of Civil Engineering, Ghent University, Technologiepark 904, Zwijnaarde B-9052, Belgium*

[2] *EPHYSLAB Environmental Physics Laboratory, Universidade de Vigo, AS LAGOAS - 32004, Ourense, Spain*

[3] *Flanders Hydraulics Research, Berchemlei 115, 2140, Antwerp, Belgium*

[4] *School of Applied Engineering and Technology, New Jersey Institute of Technology, University Heights, Newark, NJ 07102, USA*

[5] *DICATeA, University of Parma, v.le G. Usberti 181/A, 43124 Parma, Italy*

Abstract

The present work introduces the implementation of wave generation and wave absorption of non-linear, long-crested regular and irregular waves in the WCSPH-based (Weakly Compressible Smoothed Particle Hydrodynamics) DualSPHysics solver. Open boundaries are applied here for both wave generation and absorption. These boundaries consist of buffer zones, on which physical quantities are imposed, or extrapolated from the fluid domain using ghost nodes. Several layers of buffer particles are used to create an inlet and an outlet, where the horizontal component of the orbital velocities, surface elevation and pressure can be imposed from any external source or extrapolated from the fluid domain. This allows the creation of a numerical wave flume with a length of one wavelength. Reflections within the fluid domain are successfully mitigated using a velocity correction term at both inlet and outlet. The implementation is validated with theoretical solutions, in terms of water surface elevation, wave orbital velocities, and dynamic pressure. The model proves to be capable of propagating waves with less than 5% reflection, and RMSE errors on physical quantities lower than

*Corresponding author
Email address: timl.verbrugghe@ugent.be (Tim Verbrugghe [1])

4.3%. The application of open boundaries proves to be an accurate method to generate and absorb non-linear waves within a restricted domain.

Keywords: wave generation; wave propagation; wave absorption; smoothed particle hydrodynamics; open boundaries; DualSPHysics

1. Introduction

In recent years, the use of Smoothed Particle Hydrodynamics (SPH) for numerical modelling of both fundamental and engineering problems has known a steady increase. The Smoothed Particle Hydrodynamics method is a flexible Lagrangian and mesh-less technique for Computational Fluid Dynamics (CFD). The Lagrangian reference frame of SPH makes it useful in solving problems with large deformations and distorted free surfaces. In comparison with other numerical methods, the SPH formulation is simple and robust [1, 2].

This research focuses on wave propagation, wave-structure interactions and the application of SPH modeling to real engineering problems within coastal and offshore engineering. In this regard, SPH has been successfully applied to a number of free-surface problems that involve wave propagation, wave breaking and splashing [3, 4]. The impact between a rigid body and water has been studied in [5]. Wave-body interactions using an incompressible SPH (ISPH) solver have been studied in [6]. In [7], wave impact on coastal structures has been investigated. A fixed cylinder in a wave train and forced motion of cylinders generating waves are mentioned in [8], while floating bodies in waves have been successfully studied in 2-D [9]. The feasibility of applying SPH for modelling wave energy converters has been studied in [10] and [11]. 3-D problems of wave generation by a heaving cone and a floating body in waves undergoing predominantly heave motion are investigated in [12]. The latter have also indicated that simulations using a variable particle mass distribution can be beneficial.

Typically, SPH schemes are computationally intensive. However, recent advances using High Performance Computing (HPC) and Graphical Processing Units (GPU) have strongly contributed to significant gains in computational

effort [2]. Despite the use of HPC and GPUs, it is still challenging to model real engineering problems, which are usually multi-scale. An alternative to optimizing SPH for powerful computing hardware, is to study possible reduction of the computational domain. Importantly, this requires accurate and stable boundary conditions, which is one of the SPHERIC Grand Challenges (`http://spheric-sph.org/grand-challenges`). This research focuses on applying open boundary conditions within a small computational domain to accurately model wave generation and wave absorption of nonlinear regular and irregular waves, with a high accuracy.

In numerical modeling, three main types of wave generation can be distinguished [13]:

- moving boundary generation;
- internal generation;
- static boundary generation.

Of these, only the first two have been applied to SPH models [14]. Internal wave generation with a non-reflective internal wavemaker algorithm has been proposed in [15] where the Boussinesq equations are used to derive a momentum source term, which is added into an Incompressible SPH model using the Lagrangian Navier–Stokes equations. The most common wave generation method in SPH is the moving boundary generation. This mechanism tries to translate the mechanical wave generation techniques of experimental facilities directly into the numerical model. A moving boundary is implemented as a numerical wavemaker that generates and absorbs waves. Examples of this generation method can be found in [16, 9, 17, 14]. A 2-D numerical wave tank based on the open-source SPH-based DualSPHysics solver [18] was presented in [19] using analytical relaxation approach. In that work water particles inside the source generation zone move according to periodical velocities obtained from the Stokes wave theory. However, only regular wave cases were validated using this approach. Neither irregular waves nor second-order bound long waves were

simulated. Additionally, this type of wave generation technique has a higher computational cost than wave generation with moving boundaries. This is due to the large number of water particles needed in both the generation zone and the sponge layers [20]. In [21], the relaxation zone method was successfully implemented into DualSPHysics, acting as an internal wave maker and allowing coupling to other models or analytical solutions. Wen et al. [22] developed an absorbing wavemaker using the SPHysics model [23]. However, only linear wave theory was applied to generate the waves and only regular wave tests were considered. Omidvar et al. [24] used an irregular wave generation based on the linear wave theory to generate focused waves but neither super nor subharmonic components were considered in their approach. Recently, [25] presented a wave generation and absorption technique with non-reflective open boundaries, similar to the the work presented in this paper. Non-reflective boundaries have been also presented in [26] and [27] but focus more on confined flows rather than free-surface waves. Similarly, open boundary formulations for confined flow using an ISPH solver were introduced by [28] and [29] presented open boundary conditions for an SPH Shallow Water Equations model. In [30], an open boundary formulation using Riemann invariants to calculate the flow properties is introduced and applied for regular wave generation. Alternatively, wave generation in SPH can also be achieved by coupling the SPH solver to a wave propagation model. This was first demonstrated by [31], where the Boussinesq model FUNWAVE was coupled to an SPH solver to model coastal wave propagation. In [32] an ISPH solver is coupled to a quasi-arbitrary Lagrange-Euler finite element method to generate sinusoidal waves. Similarly, the SPH solver DualSPHysics was coupled to the wave propagation model SWASH in [33] and to the fully non-linear potential flow model OceanWave3D in [34].

In addition to wave generation, wave absorption is equally important in any physical or numerical model within coastal engineering. Wave absorption is specifically necessary to damp the wave energy and reduce the reflections generated by the domain boundaries. This can be done using passive wave absorber systems, which can be established by placing a gentle slope, porous

material or screens in front of the boundaries. Like this, a large amount of the incident wave energy can be dissipated. Dimensions of passive wave absorption systems typically depend on the specific wave conditions. An exponential wave damping zone was applied in [35]. In DualSPHysics, a similar algorithm is implemented and introduces a damping region in the fluid domain [14]. The numerical algorithm is very similar to application of sponge areas or porous materials in physical model tests.

Passive absorption is not sufficient when waves interact with structures; active wave absorption system is then needed. In active absorption, the wave generation method is corrected in order to remove the reflected waves present in the domain and to damp the re-reflection phenomenon. With moving wave generators, such as paddles and flaps, the corrected wavemaker displacement in function of time is obtained by transforming the original wave signal, to which an appropriate filter is applied. This filter can be a time-domain or frequency-domain filter. In literature, there are differences noticeable in the type of feedback correction signal used. In [36, 14], the free-surface elevation at the wavemaker is used, while free-surface elevation and/or orbital velocities at a fixed position in the fluid domain were used by [37]. In [38], forces acting on the wavemaker were measured and used to calculate the correction signal. The active wave absorption algorithm developed in this work applies velocity corrections to the wave generator and wave absorber, based on the measured surface elevations within the fluid domain, and thus relates the most to [36] and [14].

Typically, SPH domains for wave propagation modeling are at least 3-4 wavelengths long [33]. Combined with a required small particle size to accurately reproduce the surface elevation, this leads to computationally intensive simulations. This research is aimed at reducing the necessary fluid domain to a length of only one wavelength, and provide accurate boundary conditions capable of active wave generation and absorption. In this manner, real open sea conditions can be simulated where waves enter at the left-hand-side of the fluid domain and exit freely at the right-hand-side. The WCSPH model DualSPHysics will be

employed to demonstrate these new wave generation and wave absorption techniques, using the recently developed open boundaries [39]. The applied open boundary formulation is based on the use of buffer layers adjacent to the fluid domain. Buffer particles are used to enforce certain conditions in presence of fluid inlets and outlets. Particularly, the physical information of buffer particles is either assigned a priori or extrapolated from the fluid domain using a first order consistent procedure. The major benefits of this method are:

- Using open boundaries for wave generation and absorption is meant to cover those cases where classical wave generation techniques can fail or are very computationally expensive, e.g. open sea states, simulating floating devices, wave breaking conditions, etc.

- The buffer zones in the open boundaries accept physical information extrapolated from to fluid domain or imposed from any external source: e.g. linear wave theory, non-linear wave theories, external numerical models such as CFD models, or even measurement data.

Although a weakly compressible SPH scheme has been adopted in the present work, it is work noting that the key elements of the proposed procedure can be extended also to other types of SPH models such as Incompressible SPH [35] and/or ones based on the Arbitrarily Eulerian-Lagrangian formulation originally proposed by Vila [40].

The structure of this paper is as follows: in Section 2, the applied SPH model is described in detail. Next, the methodology of wave generation and absorption applying open boundaries is discussed in Section 3. This includes a general description of the methodology and the applied non-linear wave theories. A specification of the benchmark tests used to validate the introduced methodology is given in Section 4. In Section 5, the results of the benchmark tests are shown and discussed. In Section 6, the conclusions and future work are finally presented.

2. Smoothed Particle Hydrodynamics model

The solver used for the detailed modelling of the wave-structure interactions is DualSPHysics [18]. This section explains the theory behind the software, and is strongly based on the DualSPHysics User Guide v4.2 [41]. DualSPHysics applies the SPH formulation, a meshless method that describes the fluid as a set of discrete elements, named particles. The physical properties of a particle a, determined by the Navier-Stokes equations, can be calculated by interpolation of the values of the nearest neighbouring particles. The contribution of the neighbouring particles is weighted, based on their distance to particle a, using a kernel function W, and a smoothing length h_{SPH}.

Fundamentally, any function $F(\mathbf{r})$, defined in Γ, is estimated by integral approximation:

$$F(\mathbf{r}) = \int F(\mathbf{r'})W(\mathbf{r} - \mathbf{r'}, h_{\mathrm{SPH}})d\mathbf{r} \tag{1}$$

In order to numerically solve equation (1), discretisation is necessary. In its discrete form, the integral approximation transforms into a summation over all the particles within the region of compact support of the kernel:

$$F(\mathbf{r}_a) \approx \sum_b F(\mathbf{r}_b)W(\mathbf{r}_a - \mathbf{r}_b, h_{\mathrm{SPH}})\Delta v_b \tag{2}$$

Here, Δv_b is the volume of the neighbouring particle b. If $\Delta v_b = m_b/\rho_b$, with m and ρ being the mass and density of particle b, then equation (2) becomes:

$$F(\mathbf{r}_a) \approx \sum_b F(\mathbf{r}_b)\frac{m_b}{\rho_b}W(\mathbf{r}_a - \mathbf{r}_b, h_{\mathrm{SPH}}) \tag{3}$$

The choice of the smoothing kernel has a large influence on the performance of the SPH model. The kernel is expressed as a function of the non-dimensional distance between particles $q = r/h_{\mathrm{SPH}}$. Here, r is the distance between a certain particle a and a particle b, while h_{SPH} is the smoothing length, controlling the area around particle a in which neighbouring particles are considered. In this work, to ensure stability with a high number of particles, a Quintic kernel is applied [42] with an influence domain of $2h_{\mathrm{SPH}}$, defined as:

$$W(q, h_{\mathrm{SPH}}) = \alpha_D \left(1 - \frac{q}{2}\right)^4 (2q + 1) \qquad 0 \leq q \leq 2 \tag{4}$$

Here, α_D is equal to $7/4\pi h_{\mathrm{SPH}}^2$ (2-D). The smoothing length is set equal to $h_{\mathrm{SPH}} = 2\ d_p$ with d_p the initial particle spacing.

2.1. Governing equations

The governing equations in SPH are the Navier–Stokes equations. In its SPH formulation, the momentum conservation is expressed as:

$$\frac{d\mathbf{v}_a}{dt} = -\sum_b m_b \left(\frac{P_b}{\rho_b^2} + \frac{P_a}{\rho_a^2} + \Pi_{ab} \right) \nabla_a W_{ab} + \mathbf{g} \tag{5}$$

In equation 5, P is the pressure of the particle a or b, while ρ is the density. The viscosity term Π_{ab} is based on the artificial viscosity scheme [43] defined as:

$$\Pi_{ab} = \begin{cases} \frac{-\alpha \overline{c_{ab}} \mu_{ab}}{\overline{\rho_{ab}}} & \mathbf{v}_{ab} \cdot \mathbf{r}_{ab} < 0 \\ 0 & \mathbf{v}_{ab} \cdot \mathbf{r}_{ab} > 0 \end{cases} \tag{6}$$

With $\overline{\rho_{ab}} = 0.5(\rho_a + \rho_b)$, $r_{ab} = r_a - r_b$ and $\mathbf{v}_{ab} = \mathbf{v}_a - \mathbf{v}_b$, in which r_k is the particle position and v_k the velocity. The mean speed of sound is denoted as $\overline{c_{ab}}$ and α is a coefficient that needs to be set by the user to ensure a proper dissipation. In this work, the value of α is set to 0.01, based on [7], where wave propagation and wave loadings on coastal structures were studied.

This research applies a weakly-compressible SPH formulation (WCSPH). This means that the mass of every particle is kept constant, while only their density fluctuates. These fluctuations are calculated by solving the continuity equation, expressing the conservation of mass. In SPH formulation, this is defined by:

$$\frac{d\rho_a}{dt} = \sum_b m_b \mathbf{v}_{ab} \cdot \nabla_a W_{ab} \tag{7}$$

According to [44, 45], the relationship between density and pressure follows the so-called Tait's equation of state; a small density oscillation will lead to large pressure variations:

$$P = B \left[\left(\frac{\rho}{\rho_0} \right)^{\gamma} - 1 \right] \tag{8}$$

Here, B is related to the compressibility of the fluid, while ρ_0 is the reference density, which is set to 1000 kg/m^3 in this work. The parameter γ is the polytrophic constant, ranging between 1 and 7. Here, a value of 7 is used. The maximum limit for the density is set for $B = c^2\rho_0/\gamma$, with c the speed of sound. Consequently, the choice of B is of high importance, since it determines the value of the speed of soundwhich is artificially lowered to ensure a reasonable time step [44]. However it is advised to keep c at least 10 times faster than the maximum expected flow velocity to ensure that the fluid is weakly compressible. Here, $c = 20 * U_{max}$ with $U_{max} = \sqrt{(g * d)}$.

The time integration of the equations can be performed using a Verlet scheme or a two-stage Symplectic method. The latter is time reversible in the absence of friction or viscous effects [46]. In this work both schemes are applied. For the simple wave propagation tests, the Verlet scheme is applied, while the wave transmission and reflection tests are performed with the Symplectic method, which has an accuracy in time of $\mathcal{O}(\Delta t^2)$ and involves a predictor and corrector stage. The time step is computed according to [3] depending on the CFL number (here, CFL=0.2), the force terms and the viscous diffusion term. Additionally, the shifting algorithm introduced by [6] was applied with a threshold value of A_{FST} of 1.5.

2.2. Delta-SPH formulation

The state equation mentioned in Section 2.1 describes a very stiff density field. Unfortunately, this can lead to high-frequency low-amplitude oscillations in the density field [47]. This effect is enlarged by the natural disordering of the lagrangian particles. In order to mitigate these pressure fluctuations, the δ-SPH formulation of Molteni & Colagrossi [47] is adopted in the present work, which consists in adding a diffusive term to the continuity equation:

$$\frac{d\rho_a}{dt} = \sum_b m_b \mathbf{v}_{ab} \cdot \nabla_a W_{ab} + 2\delta_\Phi h c_0 \sum_b (\rho_b - \rho_a) \frac{r_{ab} \cdot \nabla_a W_{ab}}{r_{ab}^2} \frac{m_b}{\rho_b} \tag{9}$$

where δ_Φ is the free parameter which needs to be selected appropriately. The influence of this added term in the continuity equation has been carefully stud-

ied by [48, 49]. Within the fluid domain bulk, equation 9 represents an exact diffusive term. However, close to open boundaries such as the free surface, the behaviour changes. There, the kernel is truncated (there are no particles sampled outside of an open boundary), which results in a net first-order contribution [48]. Consequently, a net force is applied to the particles. For non-hydrostatic situations, this force is not considered relevant, since the magnitude is negligible with respect to any other involved forces. [48] did propose corrections to this effect, but they require a large computational cost since the correction involves the solution of a renormalization problem for the density gradient. Within this work, the recommended delta-SPH (δ_Φ) coefficient of 0.1 [18] is applied.

2.3. Open boundary conditions

Within this work, open boundaries are applied to generate and absorb waves. The implementation of open boundaries in DualSPHysics is discussed in detail in [39]. Inflow and outflow buffers can be defined near the inlets and outlets of the computational domain. Flow conditions can be either imposed or extrapolated from the domain interior using ghost nodes. In the latter case, variables at the ghost nodes are first calculated via a standard particle interpolation and then corrected to retrieve first order consistency. Finally, they are mirrored back to the boundary particles using Taylor series approximations.

A sketch of the implemented boundary condition model is shown in Figure 1 for a generic free-surface flow. The innermost dashed curve represents an open boundary followed by a buffer layer of particles which are used to define the boundary condition. In the case of a domain inlet, a velocity is usually imposed for the particles in the buffer such that the dot product between the assigned velocity vector and the outer normal to the inlet curve is negative. On the contrary, the inlet pressure is gathered from interpolation nodes within the fluid domain, namely ghost nodes. Particles in a buffer adjacent to a domain inlet are named inflow particles. Conversely, particles that populate the buffers adjacent to the outlets of the computational domain are called outflow particles. In the present research, the buffer width is chosen as $8 \cdot d_p$ in the direction normal

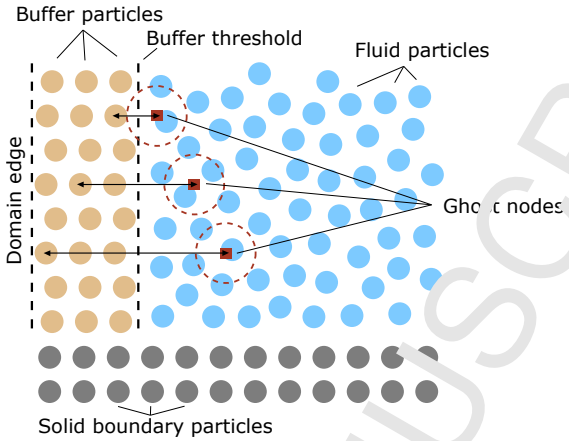

Figure 1: Sketch of the implemented open boundary model, adapted from [39].

to the open boundary, where d_p is the particle size adopted in DualSPHysics.

2.4. Dynamic boundary condition with pressure correction

The discretization of a fixed or moving solid boundary in DualSPHysics is realized through the use of dynamic boundary particles (Crespo et al. 2007). Also called dynamic boundary conditions (DBC), these have the advantage of being applicable to arbitrary 2-D and 3-D shapes, and have provided good validation in many engineering problems [50, 51]. However, the use of DBC is sometime problematic due to the unphysical density and pressure values that arise during particle interactions. Additionally, DBC exert high repulsive forces on the fluid particles, causing the formation of a gap between the fluid and the solid. In the present work, a correction is applied to the dynamic boundary particles using the working principles of the open boundary algorithm in [39]. While the velocity of the dynamic boundary particles is set to zero, the density and pressure are retrieved from the fluid domain using mirrored ghost nodes. This approach is also similar to the method used in [52]. The correction is seen to significantly mitigate the pressure oscillations in the fluid domain, and also remove the issue of the gap between the boundary and the fluid particles. The use of the correction comes with a slightly larger computational cost, in that

both the continuity and momentum equations are solved for the DBC and a unit vector normal to the DBC is calculated for each boundary particle.

3. Methodology

3.1. General Description

In this work, generation and absorption of non-linear regular and irregular waves is performed within the Weakly Compressible SPH (WCSPH) solver DualSPHysics, by applying the open boundary formulation from [39], as described in Section 2.3. The open boundaries are implemented as a zone of buffer particles. Physical quantities such as velocity, surface elevation and pressure can either be imposed on the buffer particles or extrapolated from within the fluid domain. The imposed physical quantities can originate from any source: linear or non-linear wave theories, external numerical models or even measurement data. When buffer particles cross the domain edge, they are removed from the domain. Buffer particles entering the fluid domain are transformed into fluid particles, and fluid particles entering the buffer zone become buffer particles. In the specific case an inflow buffer particle crosses the buffer-fluid interface, it becomes a fluid particle and a new buffer particle is created at the inflow boundary.

Here, a fluid domain with a length of 1 wavelength is chosen, with an inlet at the left-hand-side of the domain and an outlet at the right-hand-side of the domain (see Figure 2). Each buffer zone consists of 8 layers of buffer particles. A sensitivity analysis illustrated in Figure 3 has shown that wave propagation results are accurate for buffer zones with at least 8 layers. The dimensionless amplitude K_D is shown in function of the normalized position x/L_{wav} for a Stokes third-order wave. The number of layers n_l is varied from 1 to 16 and is doubled each iteration. It is clear that the K_D values for 8 layers and 16 layers are almost identical and the result can be considered as converged.

The imposed physical quantities originate from non-linear wave theory, detailed in Section 3.3. At the inlet, theoretical horizontal orbital velocities and

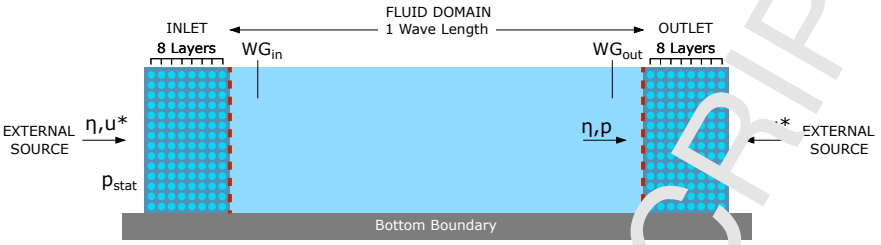

Figure 2: General sketch of numerical domain set-up to illustrate the generation/absorption methodology.

Table 1: Imposed and extrapolated quantities for inlet and outlet buffer particles (Imp=imposed, Ext=extrapolated, Stat=hydrostatic).

Quantity	u	w	η	p
inlet	Imp	0	Imp	Stat
outlet	Imp	0	Ext	Ext

surface elevation are imposed on the buffer particles, while the pressure is set to be hydrostatic, denoted p_{stat}. At the outlet, only the horizontal orbital velocities are imposed, the surface elevation and pressure are extrapolated from the fluid domain. No vertical orbital velocities are applied, analysis has proven that there is no accuracy benefit by imposing vertical velocities, but there is a negative impact on particle spacing. One drawback of imposing only the horizontal velocities in the buffer areas is the arising of a diverging velocity field near the open boundaries. However, since the area of interest will never be directly adjacent to a buffer zone, there is no negative impact on accuracy.

By imposing horizontal velocities on both the inlet and outlet, the hydrodynamic problem becomes overconstrained, which can result in unwanted reflections in the fluid domain. Additionally, when a floating or fixed structure is positioned in the fluid domain, waves will reflect on the structure and transform around it. The open boundaries should be able to compensate for the reflected waves and the outlet needs to absorb the transformed wave effectively. In this work, this is done by applying velocity corrections at the inlet and the outlet,

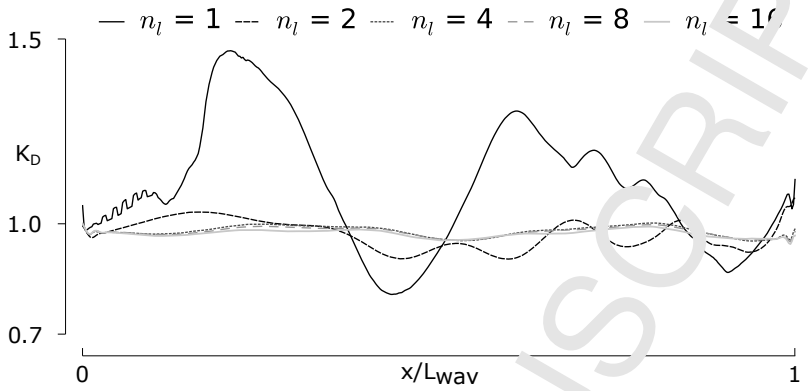

Figure 3: Sensitivity analysis on the number of buffer partic. layers n_l necessary for accurate wave propagation.

based on the measured free surface close the buffer interface, specifically at a distance of $8 \cdot d_p$. This distance has been selected based on a sensitivity analysis, illustrated in Figure 4. The same Stokes third-order wave was simulated, each time varying the wave measurement distance from $1 \cdot d_p$ to $16 \cdot d_p$. At a distance of $8 \cdot d_p$, the wave measurement location is close enough to the buffer zone to have a minimal phase difference, but far enough to avoid inaccuracies due to transitional effects between the buffer zone and the fluid domain. In Figure 2, these measuring locations are denoted as WG_{in} (Wave Gauge) and WG_{out}. The applied velocity correction is a shallow water absorption assumption based on the measured reflection [53], but is implemented differently depending on the inlet or the outlet.

3.1.1. Inlet Velocity Correction

At the inlet, the objective is to always generate the required incident wave. The surface elevation is measured directly outside of the inlet, and the velocity is corrected to ensure that the generated surface elevation matches the theoretical one. In case a higher surface elevation is measured than what was imposed, the corrected velocity should be lower than the originally imposed profile, in order to compensate the excess of velocity, since that profile leads to reflections in the

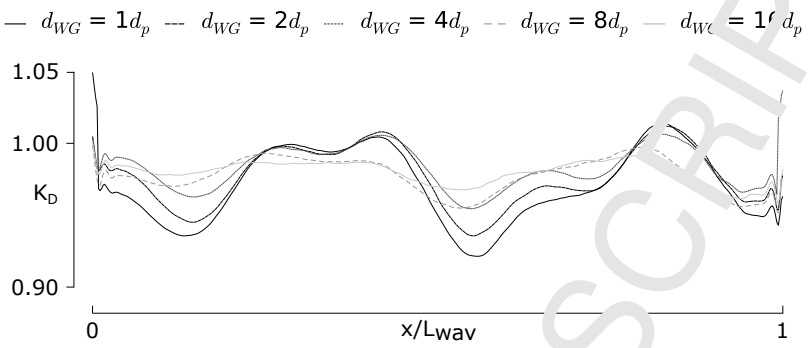

Figure 4: Sensitivity analysis on distance d_{WG} to the inlet/outlet interface of the active wave absorption wave gauges, necessary for accurate wave propagation

fluid domain. Within the code, this correction is implemented as follows:

$$u_{\mathrm{in}}(z,t) = u_{\mathrm{theory}}(z,t) - [\eta_{\mathrm{WG,in}} - \eta_{\mathrm{theory}}] \cdot \sqrt{\frac{g}{d}} \tag{10}$$

Here, $v_{\mathrm{x,in}}$ is the horizontal velocity at the inlet, $v_{\mathrm{x,theory}}$ is the imposed horizontal velocity, $\eta_{\mathrm{WG,in}}$ is the measured free surface elevation near the inlet, η_{theory} is the imposed free surface, g is the earth's acceleration and d is the water depth. This correction is similar to the active wave absorption applied in [14], although there it was used to correct the displacement of a piston-type wavemaker formed by moving boundary particles.

3.1.2. Outlet Velocity Correction

At the outlet, the objective is to absorb any wave propagating towards the outlet. Technically, the applied open boundaries do not absorb the wave, but rather try to match the velocity field present in the fluid domain as close as possible, creating an 'open door' for the propagating wave. The surface elevation is measured directly outside of the outlet, and the velocity is corrected to ensure that the imposed velocities match the measured ones. In case a higher surface elevation is measured than what was imposed, the corrected velocity should be higher than the originally imposed profile, in order to prevent discontinuities in

the velocity field, which would induce unwanted reflected waves into the domain:

$$u_{\text{out}}(z,t) = u_{\text{theory}}(z,t) - [\eta_{\text{theory}} - \eta_{\text{WG,out}}] \cdot \sqrt{\frac{g}{d}} \tag{11}$$

3.2. Implementation Into DualSPHysics

The methodology described above is implemented into the DualSPHysics source code, as illustrated in Figure 5. In the main simulation script, some minor modifications are made. At initialisation, a boolean is created to specify if active wave absorption is required or not. Additionally, it is possible to read in the theoretical surface elevations needed to calculate the velocity correction from a text file. Alternatively, these theoretical values are calculated within the DualSPHysics code itself by using newly created Stokes fifth-order functions. During the simulation, the surface elevation at WG_{in} and WG_{out} are measured and put into global variables. The theoretical surface elevations are read in from a file at discrete time intervals, and thus need to be interpolated to the current DualSPHysics timestep. If active wave absorption is required, the velocity correction is activated. Optionally, the theoretical surface elevations can be calculated here. The velocity correction is calculated as detailed in Algorithm 1 below. There, a distinction is made between an inlet and an outlet, since the velocity correction is calculated differently. A ramp function is used to smoothly introduce the velocity correction over a certain ramp time. Next, the velocity correction is calculated as discussed in equations 10 and 11. Lastly, the velocity corrections are copied to the GPU memory where they are subtracted from the original particle velocities.

3.3. Applied Non-linear Wave Theory

Both the wave generation and absorption applied in this work are based on imposing free surface and horizontal orbital velocities.

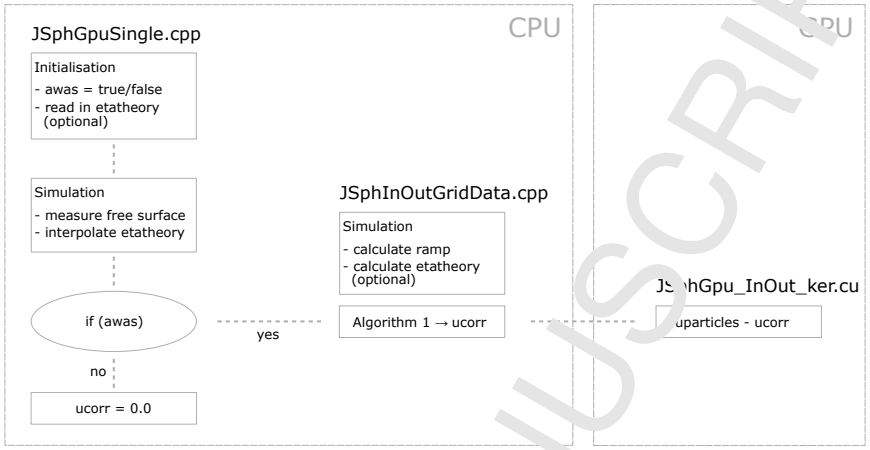

Figure 5: Implementation of velocity correction in DualSPHysics source code.

if *zone = inlet* **then**
  if *time < ramptime* **ther**
    ramp = time/ramptime;
  else
    ramp = 1.0;
  etainlet = etath ory*ramp;
  ucorr = (etamea ed-etainlet)*sqrt(g/depth);
else zone = ou
  if *time < amptime* **then**
    ra p = time/ramptime;
  else
    amp = 1.0;
  etaoutlet = etatheory*ramp;
  ucorr = (etaoutlet-etameasured)*sqrt(g/depth);
call inletoutletvelocity(other input,ucorr);

Algorithm 1: Implementation of active wave absorption in `JSphInOutGridData.cpp`.

3.3.1. Regular Waves

For regular waves, the imposed quantities are calculated with the fifth-order solution to the Stokes Theory, given by [54]:

$$k\eta(x,t) = \sum_{i=1}^{5} \epsilon^i \sum_{j=1}^{i} B_{ij} \cos[jk(x - ct + \frac{\theta}{k})] \tag{12}$$

$$\epsilon = ka \tag{13}$$

$$c = \bar{U}_c + \bar{U} \tag{14}$$

$$\bar{U}\sqrt{\frac{k}{g}} = C_0 + \epsilon^2 C_2 + \epsilon^4 C_4 \tag{15}$$

$$u(x,z,t) = \bar{U}_c + C_0\sqrt{\frac{g}{k^3}} \sum_{i=1}^{5} \epsilon^i \sum_{j=1}^{i} A_{ij} \cosh(jkz) \cos[jk(x - ct + \frac{\theta}{k})] \tag{16}$$

Here, η is the surface elevation, k is the wave number (defined as $k = 2\pi/L$, with L the wavelength), a is the wave amplitude, g is the earth acceleration, c is the wave velocity, $\bar{U}_c$ is the mean current velocity, $\bar{U}$ is the mean horizontal velocity, θ is the phase constant. The wave period T can be calculated based on the wave number k and the wave celerity c, $T = 2\pi/(kc)$. The constants A_{ij} B_{ij} and C_i are theory-specific and can be found in the appendix. The z-axis has its origin at the still water level and is negative downwards.

3.3.2. Irregular Waves

For irregular waves the surface elevation is calculated based on linear wave theory with a second-order correction, including both sub-harmonic (bound long waves) and super-harmonic components. This is done based on a Joint North Sea Wave Observation Project (JONSWAP) wave spectrum, of which 200 wave components are summed to construct the irregular surface elevation. The corresponding orbital velocities are approximated by applying the shallow water wave theory and are thus considered constant over the water depth:

$$u(x,t) = \eta_{\text{irr}}(x,t) \cdot \sqrt{\frac{g}{d}} \tag{17}$$

4. Test Program

The application of wave generation and absorption using open boundaries is hereby validated with theoretical and experimental results from the literature. Firstly, a stable non-linear standing wave is simulated by considering the outlet as a fixed wall. Secondly, simple wave propagation of regular and irregular waves is studied. Thirdly, a number of tests is performed to investigate the correct reproduction of wave transmission and wave reflection.

4.1. Standing Wave Test

First, a non-linear standing wave is simulated. A 2-D fluid domain with a water depth d and a length of 1 wavelength L_{wav} is used. An inlet is used for wave generation, while a wall is placed at the other end of the domain. If the inlet functions correctly, the applied velocity correction should ensure a stable standing wave in the fluid. This should result in visible nodes and antinodes in the surface elevation, as well as in the orbital velocities.

4.2. Wave Propagation Tests

A series of propagating waves is simulated. A 2-D fluid domain with a water depth d and a length of 1 wavelength L_{wav} is used. An inlet is used for wave generation, while an outlet handles the wave absorption (see Figure 2). The waves are selected based on their linear or non-linear characteristics, as described by the diagram of [55], adapted in Figure 6. A selection of 5 wave types is chosen, including 4 regular waves and one irregular wave. The specific characteristics such as wave height $H_{(s)}$, wave period $T_{(m)}$, water depth d and particle size d_p are listed in Table 2. The particle size is selected based on the rule of thumb that $d_p \leq H/10$, as demonstrated in [14] and [56]. The validity of the regular wave theories is illustrated in Figure 6. The accuracy of the wave propagation is assessed by comparing surface elevation, orbital velocities and dynamic pressures with theoretical results.

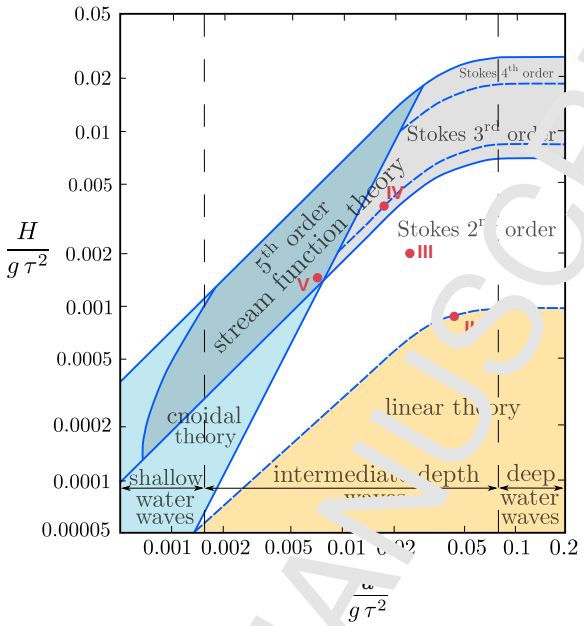

Figure 6: Selection of waves tested with the two-way coupled model. Tests II-V are indicated on the graph (adapted from [55]). The normalized water depth is denoted as $\frac{d}{g\tau^2}$, while $\frac{H}{g\tau^2}$ is the normalized wave height.

4.3. Wave Transmission Tests

Next, a combination of wave reflection and wave transformation is studied by simulating wave propagation over a submerged breakwater with a smooth impermeable slope (see Figure 7). Part of the wave will reflect on the breakwater, while part of the wave will be transmitted over the breakwater. A fluid domain with a water depth of d and length of $2 \cdot L_{\text{wav}}$ is selected. An inlet is used for wave generation, while an outlet handles the wave absorption. The submerged breakwater is positioned midway along the length, has a height of h_{bw} and a slope of 1/1.5. The ratio d/h_{bw} is equal to 1.2. Validation of this test case is obtained by comparing the transmission coefficient $C_T = \frac{H_t}{H_i}$ with results from [57].

Table 2: Wave Propagation Tests: Wave Conditions.

Test Number	**Wave Theory**	**Wave Height** $\mathbf{H}_{(s)}$ **[m]**	**Wave Period** $\mathbf{T}_{(m)}$ **[s]**	**Water Depth** **d [m]**	**Wave Length** **L [m]**	**Particle Size** d_p **[m]**
I	Standing	0.15	2.0	0.7	4.62	0.020
II	Linear	0.02	1.5	1.0	3.35	0.0020
III	Stokes 2^{nd}	0.08	2.0	1.0	5.22	0.010
IV	Stokes 3^{rd}	0.15	2.0	0.7	4.62	0.010
V	Stream Function	0.06	2.0	0.3	3.26	0.005
VI	Irregular Wave	0.15	2.0	1.0	/	0.01

4.4. Wave Reflection Tests

Lastly, wave reflection tests are carried out by propagating irregular waves on smooth impermeable breakwaters with varying slopes (see Figure 8). The domain consists of a fluid section with a water depth d and a length of 1 wavelength L_{wav}. A smooth impermeable breakwater with slope angle α is installed at the right side of the domain. Validation of the test case is achieved by calculating the reflection coefficient C_R with WaveLab, and comparing the result to the formula of [58]:

$$C_R = \frac{a\xi}{b + \xi^2} \qquad \xi = \frac{\tan\alpha}{\sqrt{\frac{2\pi H}{gT^2}}} \tag{18}$$

Equation (18) is valid for values of ξ ranging from 2.0 to 6.0. For the wave conditions used in this test case, this results in slope angles between 20° and 45°.

5. Results and Discussion

5.1. Standing Wave Test

The accuracy of wave propagation with open boundaries is assessed by comparing SPH surface elevation and orbital velocities with the corresponding theoretical results, as illustrated in Figure 9. The first graph shows the comparison

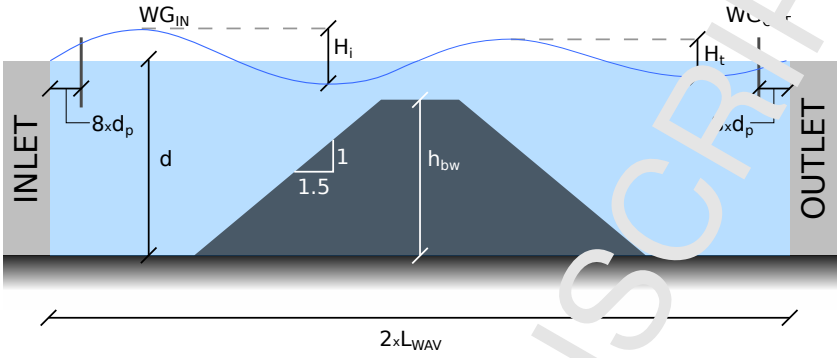

Figure 7: Set-up of wave transmission tests with submerged breakwaters and smooth impermeable slopes.

of the surface elevation, the second graph the horizontal orbital velocities and the third graph the vertical orbital velocities. The theoretical standing wave was calculated as a Stokes 2^{nd} order standing wave. For a perfectly linear standing wave pattern, the free-surface elevation should be zero at the nodes and twice the amplitude of the incident waves at the antinodes. As visible in 9, a perfect pattern is not achieved, since we have simulated a non-linear standing wave. The amplitudes at the nodes are very small (maximum 2 cm) as predicted by the second-order solution and the amplitudes at the antinodes are close to their maximum. Both the horizontal and vertical orbital velocities show good agreement with the theoretical result.

5.2. Wave Propagation Tests

The accuracy of wave propagation with open boundaries is now assessed by comparing the free surface elevation, orbital velocities and dynamic pressures with the corresponding theoretical results.

5.2.1. Surface Elevations

The surface elevation for the regular waves, measured at the center of the domain is compared to the theoretical surface elevation in Figure 10. It is clear

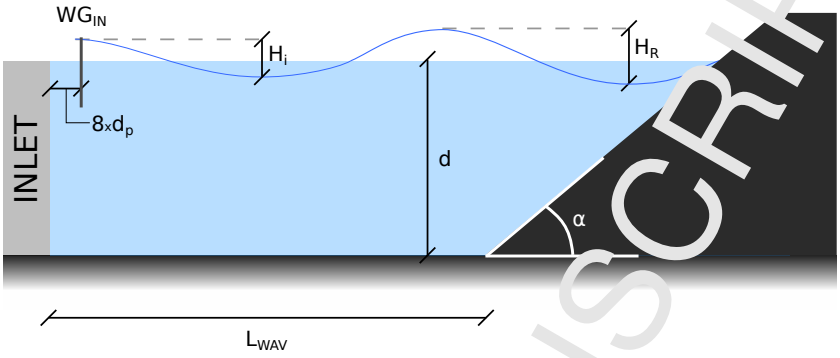

Figure 8: Set-up of wave reflection tests on breakwater with a smooth impermeable slope.

that the surface elevation is simulated with a very high accuracy. Both the wave crest and wave through are reproduced excellently. Additionally, the asymmetry of the non-linear wave types is preserved well. In order to quantify the accuracy, RMSE values are calculated as follows:

$$RMSE = \frac{\sqrt{\frac{1}{n}\sum_{i=1}^{n}(\eta_{\mathrm{SPH}} - \eta_{\mathrm{theory}})^2}}{h_{\mathrm{SPH}}} \qquad h_{\mathrm{SPH}} = 1.2 \cdot d_p \cdot \sqrt{2} \tag{19}$$

This is a specific RMSE calculation for SPH simulations, where the error is non-dimensional with respect to the smoothing length h_{SPH}. Results are considered acceptable when the RMSE value is lower than one. In Table 3, the RMSE values for the surface elevation of the propagating wave tests are given. The calculated errors are low and range from 13.9% for wave V to 17.5% for wave III, proving that the applied wave generation and absorption technique is capable of accurately reproducing the surface elevation of linear and non-linear waves.

Table 3: RMSE values for surface elevations of wave types II-V.

Wave Test	II	III	IV	V
RMSE	0.169	0.175	0.172	0.139

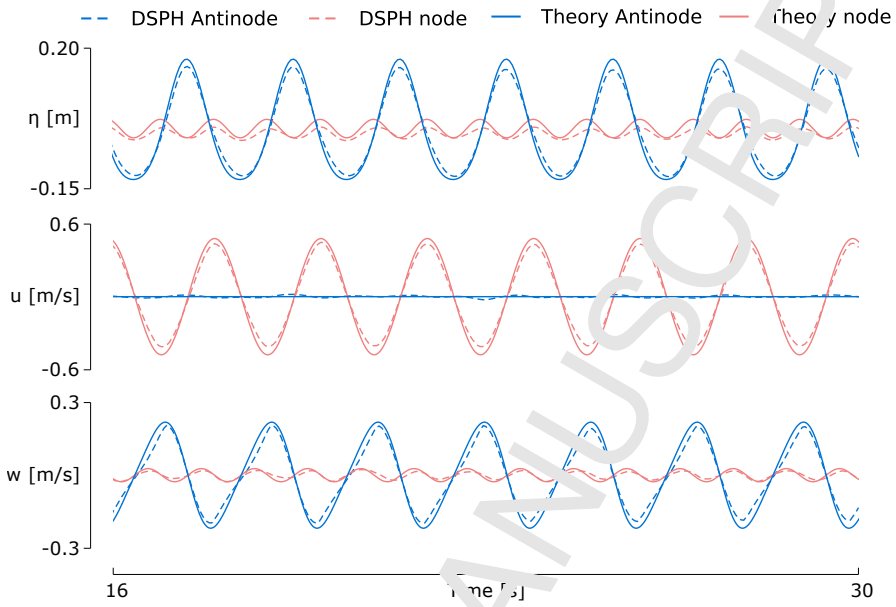

Figure 9: Comparison of surface elevation η (top), horizontal orbital velocity u (middle) and vertical orbital velocity w (bottom) in nodes and antinodes for a non-linear standing wave.

Additionally, the dimensionless amplitude K_D is calculated as follows:

$$K_D = \sqrt{\frac{8 \cdot \sum_{i=0}^{n_t} \eta_i^2}{H \cdot n_t}} \tag{20}$$

Here, n_t is the number of time steps. The K_D value is calculated for waves II-V and plotted as a function of the domain length in Figure 11. It is clear that the reflections in the domain are minimal, with K_D values ranging from 0.95 to 1.02.

Lastly, the propagation of an irregular wave with $H_s = 0.15$ m and $T_m = 2.0$ s was simulated. The accuracy of the simulation is determined by performing a reflection analysis with WaveLab on an irregular wave train of 500 waves. The analysis is based on the N-gauge extension of the 3-gauge Mansard and Funke method, as presented in [59]. The result is illustrated in Figure 12, where the incident spectrum S_{incident}, the reflected spectrum $S_{\text{reflected}}$, and the reflection coefficient C_R are given. Around the peak frequency of $0.39Hz$, reflection is

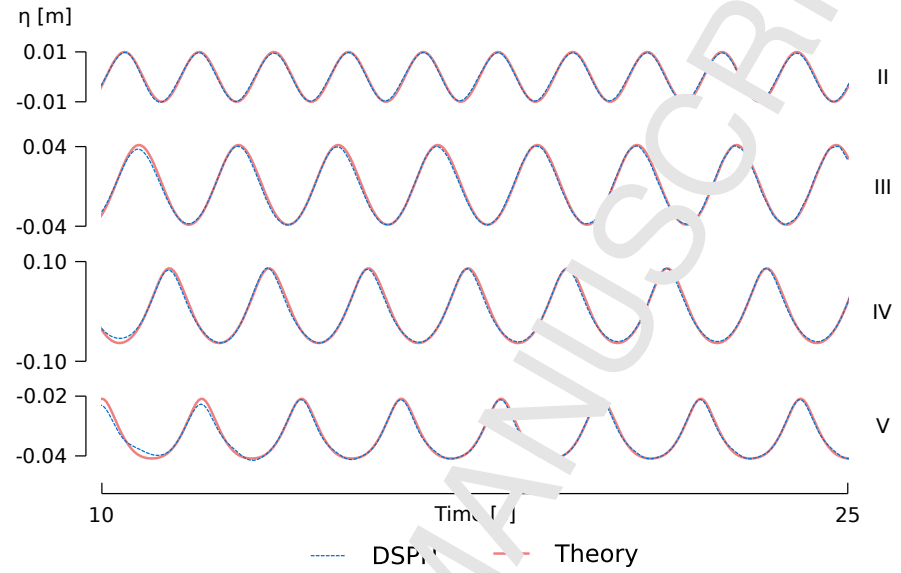

Figure 10: Surface elevations of wave tes[illegible]II-V, measured in the center of the fluid domain $x = L_{\text{wav}}/2$.

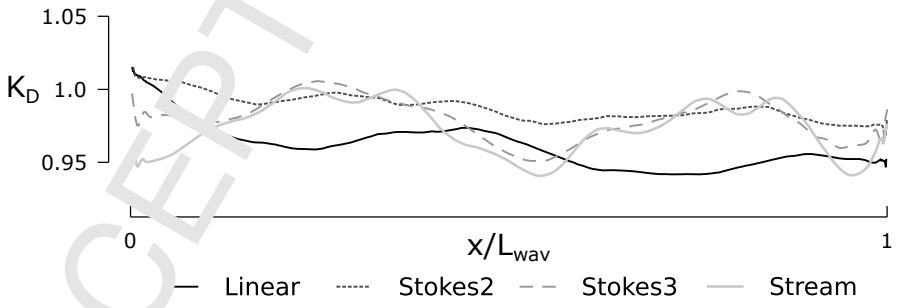

Figure 11: Dimensionless amplitude wave tests II-V.

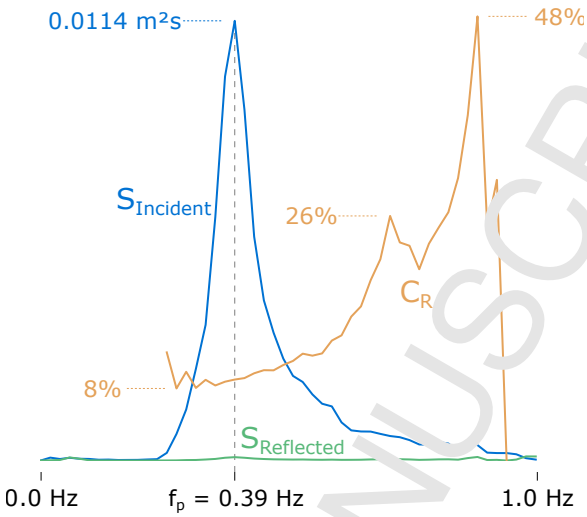

Figure 12: Reflection analysis of regular wave.

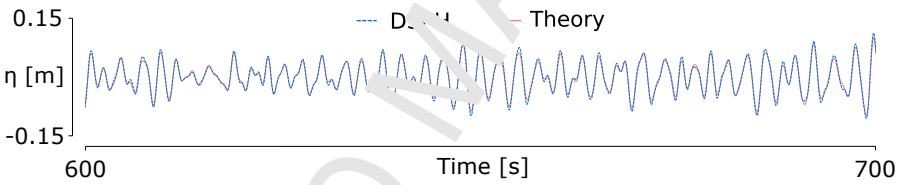

Figure 13: Surface elevation comparison between theoretical and numerical result, measured in the middle of the domain.

very low with C_R ranging from 8% to 11%. Towards the higher frequencies, C_R rises up to 26%. However, the spectral density from these high-frequency components is very low, and the impact on the accuracy of the surface elevation is minimal. Next to a frequency analysis, the surface elevation can be compared in the time domain. A visual representation of the comparison of the surface elevation between the theoretical and numerical results is visible in Figure 13. It is clear that DualSPHysics with the current open boundary formulation can properly propagate non-linear irregular waves.

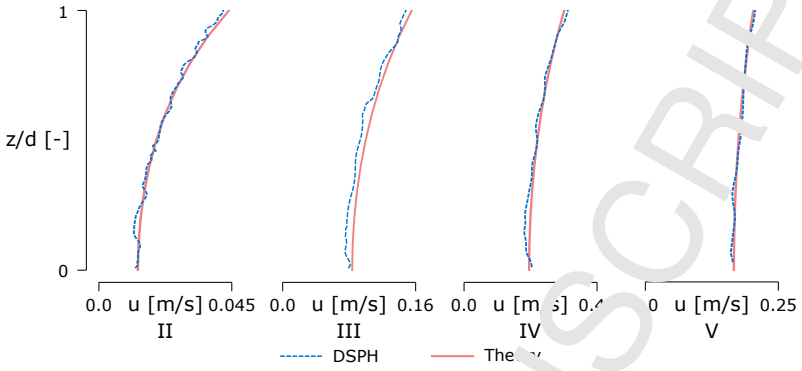

Figure 14: Comparison of horizontal orbital velocities of simulated waves to non-linear wave theory.

5.2.2. Orbital Velocities

A propagating wave is not only characterized by its surface elevation, but also by the orbital velocities in the horizontal and vertical directions. In Figure 14, the horizontal orbital velocities under a wave crest are compared to theoretical results, while the vertical orbital velocities are compared in Figure 15. Despite some small oscillations, probably due to the small artificial viscosity parameter alpha herein adopted, DualSPHysics is capable of accurately reproducing the horizontal and vertical orbital velocities. In order to quantify the accuracy, RMSE values are calculated as follows:

$$RMSE = \frac{\sqrt{\frac{1}{n}\sum_{i=1}^{n}(u_{\mathrm{SPH}} - u_{\mathrm{theory}})^2}}{max(u_{\mathrm{theory}})} \tag{21}$$

The results for each Wave Test are summarized in Table 4. The RMSE values range from 1.5% to 4.3%, proving the high accuracy of wave generation, propagation and absorption.

Table 4: RMSE values for orbital velocities of wave types II-V.

Wave Test	II	III	IV	V
$\mathbf{RMSE}_u$	0.023	0.043	0.027	0.015
$\mathbf{RMSE}_w$	0.021	0.024	0.026	0.018

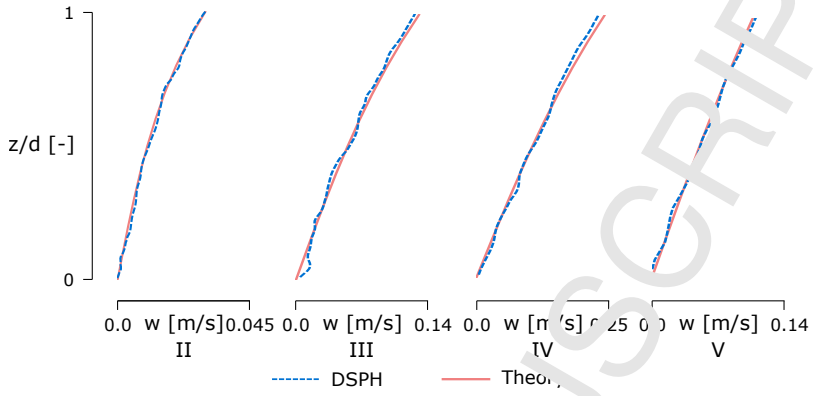

Figure 15: Comparison of vertical orbital velocities of simulated waves to non-linear wave theory.

5.2.3. Pressure

Herein the pressure distribution obtained with SPH is compared to the corresponding pressure profile from theory. The results are shown in Figure 16, where the mean total pressure, $\overline{p}(z)$, and its standard deviation are plotted as a function of the vertical position, z, at a certain time, t_i, and at the middle section $x_s = L_{\text{wav}}/2$. The solid line represents the value of $\overline{p}(z)$ while the shaded area is indicative of standard deviation, calculated as:

$$\overline{p}(z) = \frac{1}{n_t} \sum_{t_i=0}^{t_{\text{sim}}} p(x_s, z, t_i) \tag{22}$$

$$\sigma_p(z) = \sqrt{\frac{1}{n_t} \sum_{t_i=0}^{t_{\text{sim}}} \left(p(x_s, z, t_i) - \overline{p}(z)\right)^2} \tag{23}$$

Here, p is the total pressure at a certain point (x_s, z) at a certain time t_i. The standard deviation is directly related to the added dynamic pressure due to the wave action. The wave tests III, IV and V have excellent agreement, while wave test II has a slightly curved pressure distribution. Wave test IV has the highest wave height of $0.15m$, leading to higher pressure fluctuations and higher velocities of the buffer particles. Again, the RMSE values are calculated for the mean total pressure as $RMSE_p = \sqrt{\frac{1}{n}\sum_{i=1}^{n}(p_{\text{sim}} - p_{\text{theory}})^2}/max(p_{\text{theory}})$, see

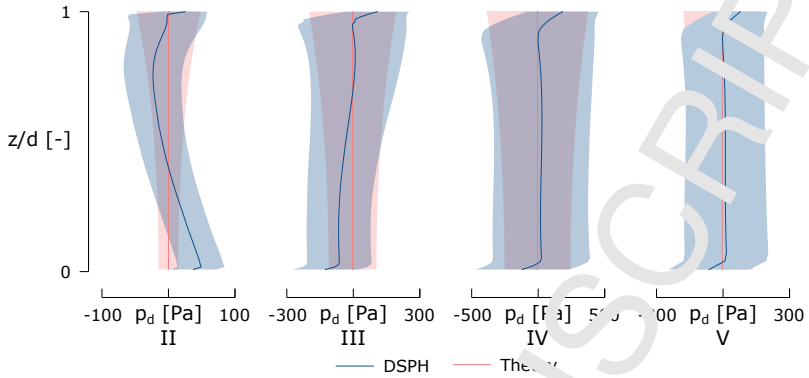

Figure 16: Comparison of dynamic pressure of tested waves. The solid line represents the mean total pressure while the shaded area represents the standard deviation

Table 5. The RMSE values for all 4 waves are low, ranging from 0.002 to 0.008, with the best performance for wave type II and the worst performance for wave type V. It is remarked that the RMSE values are low because the total pressure is considered here rather than the dynamic pressure.

Table 5: RMSE values for mean total pressure of wave types II-V.

Wave Test	II	III	IV	V
RMSE$_p$	0.002	0.004	0.006	0.008

5.2.4. Computational Speed-up

One of the main benefits of applying open boundaries is to have a relatively small domain for open sea states where waves need to freely propagate through the domain without any reflections. While classic wave propagation simulations in SPH require a domain length of 3-4 wavelengths, the domain here can be only 1 wavelength long. This leads to a significant reduction in computational effort and cost. In order to quantify the achievable computational speed-up, the number of particles and the simulation runtime are compared between the new open boundary method and a classic wave propagation simulation with a flume length of 4 wavelengths. Based on this rule of thumb, the classic simulations

are run and compared to new method in Table 6. The comparison between the number of particles results in a theoretical speed-up. However, the runtime comparison indicates that there can be a difference between the theoretical speed-up and effective computational speed-up. Nevertheless, it is clear that a significant computational speed-up is possible by using open boundaries and a reduced domain size. The effective computational speed-up ranges from 146% to 727%.

Table 6: Computational speed-up for wave propagation tests.

	Time [hr]			# Particles		
Wave Test	**Classic Method**	**New Method**	**Computational Speed-up**	**Classic Method**	**New Method**	**Theoretical Speed-up**
II	39.33	14.38	273%	2 442k	1512k	162%
III	3.74	0.51	727%	434k	89k	487%
IV	0.83	0.42	197%	260k	66k	396%
V	1.30	0.89	146%	301k	144k	209%

5.3. Wave Transmission Test

A number of regular waves are hereby propagating towards a submerged breakwater with a smooth, impermeable slope of 1/1.5. Part of the waves reflects on the structure, while another part of the wave energy is transmitted over the breakwater. This results in a reduction of the wave height behind the breakwater. The accuracy of the simulations is quantified by comparing the calculated transmission coefficient, C_T, with the theoretical values published in [57]. The comparison is illustrated in Figure 17. Since there are some fluctuations in the measured wave height in the lee of the submerged breakwater, the average transmission coefficient is calculated and plotted together with the measured standard deviation. In the left graph, the theoretical relation between the dimensionless wave height H/gT^2 and the transmission coefficient C_T is compared to the simulated data. Simulations were performed with 4 wave

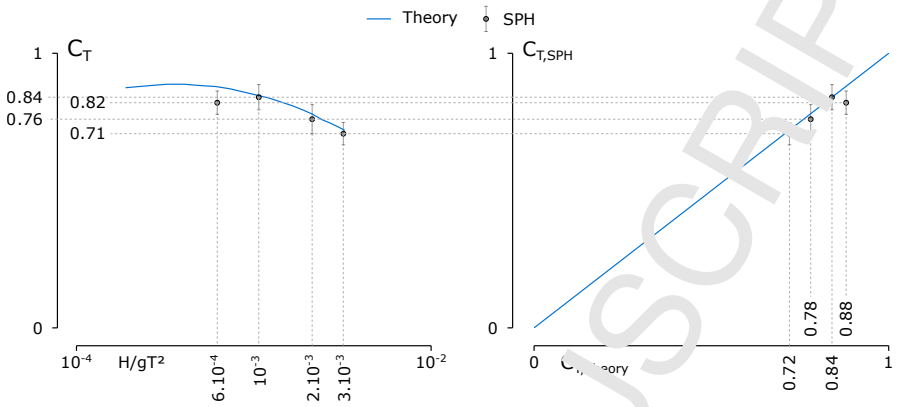

Figure 17: Comparison of simulated transmission coefficient $C_{T,SPH}$ and theoretical transmission coefficient $C_{T,Theory}$.

heights, ranging from $0.035m$ to $0.18m$. Lower wave heights would result in a too small particle size and thus a too long computation time. The accuracy is good with errors on C_T ranging from 1% to 4%. The right graph illustrates this by comparing the measured and theoretical transmission coefficient directly.

5.4. Wave Reflection Tests

An irregular wave train of 500 waves is propagated towards a breakwater with a smooth, impermeable slope. Part of the waves reflects on the structure, while another part of the wave energy dissipates due to breaking and run-up. The accuracy of the simulations is quantified by comparing the calculated reflection coefficient C_R with the theoretical values published in [58]. The comparison is illustrated in Figure 18. In the left graph, the theoretical relation between the slope angle α and the reflection coefficient C_R is compared to the simulated data. Simulations were performed with 6 slope angles, ranging from 20° to 45° with a step of 5°. The accuracy is good with errors on C_R ranging from 1.2% to 6.8%. The right graph illustrates this by comparing the measured and theoretical reflection coefficient directly.

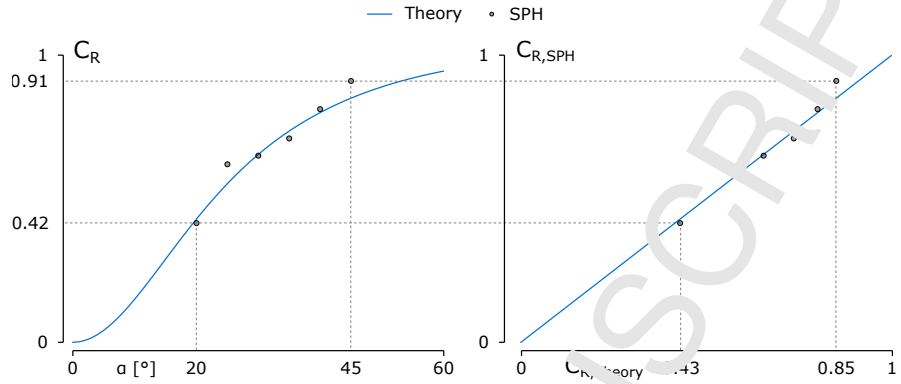

Figure 18: Comparison of simulated reflection coefficient $C_{R,SPH}$ and theoretical reflection coefficient $C_{R,Theory}$.

6. Conclusions

In this paper, a novel wave generation and absorption method using open boundaries was introduced. A fluid domain of one wavelength long is selected, with an inlet and outlet composed of 8 buffer particle layers at both sides. At the inlet, theoretical horizontal velocity and surface elevation are imposed to the buffer particles, while the pressure is extrapolated from ghost nodes placed in the fluid domain. At the outlet, only theoretical horizontal velocity is imposed, while pressure and surface elevation are extrapolated from the fluid domain. At both the inlet and outlet, a custom velocity correction algorithm is applied, based on measuring the reflected wave and calculating the corrected velocity based on shallow water wave theory. The introduced generation and absorption methodology is applied to the WCSPH solver DualSPHysics. The methodology is validated by comparing simulation results to theoretical results and results from literature. Generally, wave generation/absorption with open boundaries has the following benefits:

- The computation time can be significantly smaller for open sea simulations where no reflections are present since a fluid domain of only one wavelength long is sufficient for accurate wave propagation. Cases where this is of

high interest are, for example, simulations of floating structures/devices such as Wave Energy Converters, offshore floating wind platforms, etc. Alternatively, for the same computation time as a typical SPH simulation with moving boundaries and a domain length of 3-4 wavelengths [33], there is the possibility of simulating more particles for a higher accuracy (see also Table 6).

- The quantities imposed on the buffer particles can come from any type of external sources:: linear or non-linear wave theories, other numerical models such as CFD models, potential flow models, Boussinesq models, and measurement data could be imposed.

- Due to the automatic insertion and removal of buffer particles through the boundary lines, there are no issues with preserving mass conservation due to Stokes drift.

Though the open boundary formulation implemented in DualSPHyiscs by [39] has been shown to properly simulate wave generation and absorption, this methodology will be further expanded. The extension of the algorith to a $3-D$ environment needs to be tested and validated thoroughly. Next, The methodology will be applied to simulate scale models of floating wave energy converters, and validated with experimental data. Additionally, a study will investigate if the inlet can be used in a region where classic piston-type wave generation fails, e.g. close to a wave breaking zone. If this is the case, large computational gains are predicted. Finally, research will be performed into more complex shapes of the buffer zones, such as circular zones acting as inlet and outlet simultaneously. The upgraded methodology will be thoroughly tested and compared to theoretical solutions and experimental datasets.

Acknowledgements

This work was supported by the Agency for Innovation by Science and Technology in Flanders (IWT/Vlaio) with the scholarship 141402. This work

was also partially financed by Xunta de Galicia (Spain) under project ED431C 2017/64 Programa de Consolidación e Estructuración de Unidades de Investigaciósn Competitivas (Grupos de Referencia Competitiva) co-funded by European Regional Development Fund (FEDER) and by Xunta de Galicia postdoctoral grant ED481B-2018/020. The work was also funded by the Ministry of Economy and Competitiveness of the Government of Spain under project WELCOME ENE2016-75074-C2-1-R and by EU under FRDF (European Regional Development Fund) through the Interreg project MaRRISK (0262-MARRISK-1-E). This work was partially supported by the Italian Ministry of Education, University and Research (MUIR) under the Scientific Independence of Young Researchers project, grant number RBSI14R1GP, CUP code D92I15000190001

References

[1] J. J. Monaghan, Reports on progress in physics 68 (2005) 1703.

[2] H. Gotoh, A. Khayyer, Coastal Engineering Journal 0 (2018) 1–25. doi:10.1080/21664250.2018.1436243.

[3] J. Monaghan, A. Kos, Journal of waterway, port, coastal, and ocean engineering 125 (1999) 145–155.

[4] R. Dalrymple, B. Rogers, Coastal engineering 53 (2006) 141–147.

[5] J. Monaghan, A. Kos, N. Issa, Journal of Waterway, Port, Coastal, and Ocean Engineering 129 (2003) 250–259.

[6] A. Skillen, S. Lind, P. K. Stansby, B. D. Rogers, Computer Methods in Applied Mechanics and Engineering 265 (2013) 163 – 173. URL: http://www.sciencedirect.com/science/article/pii/S0045782513001448. doi:http://doi.org/10.1016/j.cma.2013.05.017.

[7] C. Altomare, A. J. Crespo, J. M. Domínguez, M. Gómez-Gesteira, T. Suzuki, T. Verwaest, Coastal Engineering 96 (2015) 1–12. doi:10.1016/j.coastaleng.2014.11.001.

[8] P. Omidvar, P. K. Stansby, B. D. Rogers, International Journal for Numerical Methods in Fluids 68 (2012) 686–705.

[9] S. Manenti, A. Panizzo, P. Ruol, L. Martinelli, in: Proceedings of 3rd SPHERIC Workshop, pp. 38–41.

[10] T. Verbrugghe, B. Devolder, J. Domínguez, A. Kortenhaus, P. Troch, in: Proceedings of the 12th wave and tidal energy conference, pp. 679–689.

[11] A. Crespo, C. Altomare, J. Domínguez, J. González-Cao, M. Gómez-Gesteira, Coastal Engineering 126 (2017) 11–26.

[12] P. Omidvar, P. K. Stansby, B. D. Rogers, International Journal for Numerical Methods in Fluids 72 (2013) 427–452.

[13] P. Higuera, I. J. Losada, J. L. Lara, Coastal Engineering 101 (2015) 35–47.

[14] C. Altomare, J. Domínguez, A. Crespo, J. González-Cao, T. Suzuki, M. Gómez-Gesteira, P. Troch, Coastal Engineering 127 (2017) 37–54.

[15] P. Lin, P. L.-F. Liu, Journal of waterway, port, coastal, and ocean engineering 125 (1999) 207–215.

[16] E. Didier, M. Neves 22 (2012) 193–199.

[17] D. D. Meringolo, F. Aristodemo, P. Veltri, Coastal Engineering 101 (2015) 48–68.

[18] A. Crespo, J. Domínguez, B. Rogers, M. Gómez-Gesteira, S. Longshaw, R. Canelas, R. Vacondio, A. Barreiro, O. García-Feal, Computer Physics Communications 187 (2015) 204–216. doi:10.1016/j.cpc.2014.10.004.

[19] X. Y. Ni, W. B. Feng, Applied Mechanics and Materials 405-408 (2013) 1463–1471. URL: http://www.scientific.net/AMM.405-408.1463. doi:10.4028/www.scientific.net/AMM.405-408.1463.

[20] X. Ni, W. Feng, D. Wu, International Journal for Numerical Methods in Fluids 76 (2014) 223–245.

[21] C. Altomare, B. Tagliafierro, J. Domínguez, T. Suzuk[illegible] G[illegible] Viccione, Applied Ocean Research 81 (2018) 15 – 33. URL: http://www.sciencedirect.com/science/article/pii/S014[illegible]718303705. doi:https://doi.org/10.1016/j.apor.2018.09.013.

[22] H. Wen, B. Ren, P. Dong, Y. Wang, Applied Ocean Research 59 (2016) 366–377.

[23] M. Gomez-Gesteira, B. D. Rogers, A. J. Crespo, [illegible]. A. Dalrymple, M. Narayanaswamy, J. M. Domínguez, Computers & Geosciences 48 (2012) 289–299.

[24] P. Omidvar, P. K. Stansby, B. D. Rogers, International Journal for Numerical Methods in Fluids 72 (2013) 427–452.

[25] X. Ni, W. Feng, S. Huang, Y. Zhang, X. Feng, Ocean Engineering 163 (2018) 483 – 50[illegible] URL: http://www.sciencedirect.com/science/article/pii/S[illegible]1818310588. doi:https://doi.org/10.1016/j.oceaneng.2018.06.034.

[26] M. Lastiwka, M. Bas[illegible] N. J. Quinlan, International Journal for Numerical Methods in Fluids 61 (200[illegible]) 709–724. URL: https://onlinelibrary.wiley.com/doi/a[illegible]s/10.1002/fld.1971. doi:10.1002/fld.1971. arXiv:https://onlinelibrary.wiley.com/doi/pdf/10.1002/fld.1971.

[27] C. E. Alva[illegible]-Rodríguez, J. Klapp, L. D. G. Sigalotti, J. M. Domínguez, E. de la Cruz Sánchez, Computers & Fluids 159 (2017) 177 – 188. doi:https://doi.org/10.1016/j.compfluid.2017.09.020.

[28] S. Khora[illegible]zade, J. M. M. Sousa, International Journal for Numerical Methods in Fluids 80 (2016) 161–180. URL: https://onlinelibrary.wiley.com/doi/abs/10.1002/fld.4074. doi:10.1002/fld.4074. arXiv:https://onlinelibrary.wiley.com/doi/pdf/10.1002/fld.4074.

[29] R. Vacondio, B. D. Rogers, P. K. Stansby, International Journal for Numerical Methods in Fluids 69 (2012) 226–253. URL: http://doi.wiley.com/10.1002/fld.2559. doi:10.1002/fld.2559.

[30] M. Ferrand, A. Joly, C. Kassiotis, D. Violeau, A. Leroy, F.-X. Morel, B. D. Rogers, Computer Physics Communications 210 (2017) 29–44. URL: https://ac.els-cdn.com/S0010465516302806/1-s2.0-S0010465516302806-main.pdf?{_}tid=41db2578-fc5a-11e7-997d-00000aacb0f26{&}acdnat=1516285204{_}328024bdee3d092ce9a956ae61e4d263. doi:10.1016/j.cpc.2016.09.009.

[31] M. Narayanaswamy, A. J. C. Crespo, M. Gómez-Gesteira, R. A. Dalrymple, Journal of Hydraulic Research 48 (2010) 85–93.

[32] G. Fourtakas, P. K. Stansby, B. D. Rogers, S. J. Lind, S. Yan, Q. W. Ma, et al., in: The 27th International Ocean and Polar Engineering Conference, International Society of Offshore and Polar Engineers.

[33] C. Altomare, J. M. Domínguez, A. J. C. Crespo, T. Suzuki, I. Caceres, M. Gómez-Gesteira, Coastal Engineering Journal 57 (2016) 1–34. doi:10.1142/S0578563415500242.

[34] T. Verbrugghe, J. M. Domínguez, A. J. Crespo, C. Altomare, V. Stratigaki, P. Troch, A. Kortenhaus, Coastal Engineering 138 (2018) 184–198. doi:10.1016/j.coastaleng.2018.04.021.

[35] S. Lind, R. Xu, P. Stansby, B. Rogers, Journal of Computational Physics 231 (2012) 1499–1523. doi:10.1016/j.jcp.2011.10.027.

[36] L. A. Schäffer, G. Klopman, Journal of waterway, port, coastal, and ocean engineering 126 (2000) 88–97.

[37] P. Frigaard, M. Christensen, in: Coastal Engineering 1994, 1995, pp. 168–180.

[38] S. H. Salter, Proceedings of the Conference on Directional Wave Applications.

[39] A. Tafuni, J. Domínguez, R. Vacondio, A. Crespo, Computer Methods in Applied Mechanics and Engineering 342 (2018) 604–624. URL: http://www.sciencedirect.com/science/article/pii/S0045782518303906. doi:https://doi.org/10.1016/j.cma.2018.08.004.

[40] J. P. VILA, Mathematical Models and Methods in Applied Sciences 09 (1999) 161–209. doi:10.1142/S0218202599000117. arXiv:https://doi.org/10.1142/S0218202599000117.

[41] A. Crespo, J. Domínguez, M. Gómez-Gesteira, A. Barreiro, B. Rogers, University of Vigo. The University of Manchester and Johns Hopkins University (2018).

[42] H. Wendland, Advances in computational Mathematics 4 (1995) 389–396.

[43] J. J. Monaghan, Annual review of astronomy and astrophysics 30 (1992) 543–574.

[44] J. J. Monaghan, Journal of computational physics 110 (1994) 399–406.

[45] G. K. Batchelor, An introduction to fluid dynamics, Cambridge university press, 2000.

[46] B. J. Leimkuhler, S. Reich, R. D. Skeel, IMA Volumes in Mathematics and its Applications 82 (1996) 161–186.

[47] D. Molteni, A. Colagrossi, Computer Physics Communications 180 (2009) 861 – 872. doi:https://doi.org/10.1016/j.cpc.2008.12.004.

[48] M. Antuono, A. Colagrossi, S. Marrone, Computer Physics Communications 183 (2012) 2570 – 2580. doi:https://doi.org/10.1016/j.cpc.2012.07.006.

[49] M. D. Green, R. Vacondio, J. Peiró, Computers & Fluids 179 (2019) 632 – 644. URL: http://www.sciencedirect.com/science/article/pii/S0045793018309009. doi:https://doi.org/10.1016/j.compfluid.2018.11.020.

[50] A. Tafuni, I. Sahin, Journal of Fluids and Structures 52 (2015) 101 – 117. URL: http://www.sciencedirect.com/science/article/pii/S0889974614002199. doi:https://doi.org/10.1016/j.jfluidstructs.2014.10.004.

[51] C. Altomare, A. J. Crespo, B. Rogers, J. Domínguez, X. Gironella, M. Gómez-Gesteira, Computers & Structures 130 (2014) 34–45.

[52] S. Marrone, M. Antuono, A. Colagrossi, G. Colicchio, D. L. Touzé, G. Graziani, Computer Methods in Applied Mechanics and Engineering 200 (2011) 1526 – 1542. doi:https://doi.org/10.1016/j.cma.2010.12.016.

[53] R. G. Dean, R. A. Dalrymple, Water wave mechanics for engineers and scientists, volume 2, world scientific publishing Co Inc, 1991.

[54] J. D. Fenton, Journal of waterway, port, coastal, and ocean engineering 111 (1985) 216–234.

[55] B. Le Méhauté, Oceanic fronts in Coastal Processes (1969) 114.

[56] R. A. R. Roselli, G. Vernengo, C. Altomare, S. Brizzolara, L. Bonfiglio, R. Guercio, Environmental Modelling & Software 103 (2018) 62–73.

[57] W. N. Seelig, Estimation of Wave Transmission Coefficients for Overtopping of Impermeable Breakwaters., Technical Report, COASTAL ENGINEERING RESEARCH CENTER FORT BELVOIR VA, 1980.

[58] W. Seelig, in: Proceedings of coastal structures 1983 Conference, Arlington, USA, ASCE, New York, pp. 961–973.

[59] J. Zelt, J. E. Skjelbreia, Estimating Incident and Reflected Wave Fields Using an Arbitrary Number of Wave Gauges, 1992. doi:10.1061/9780872629332.058.

Appendix A. Fifth-Order Wave Theory Constants

Here, the constants A_{ij} B_{ij} and C_i, necessary to calculate the surface elevation and orbital velocities with the Stokes 5^{th} Order Wave Theory in a water depth D are given:

$$S = \frac{\cosh 2kD}{\sinh 2kD}$$

$$A_{11} = 1/\sinh(kD)$$

$$A_{22} = 3S^2/[2(1-S)^2]$$

$$A_{31} = (-4 - 20S + 10S^2 - 13S^3)/[8\sinh(kD)(1-S)^3]$$

$$A_{33} = (-2S^2 + 11S^3)/[8\sinh(kD)(1-S)^3]$$

$$A_{42} = (12S - 14S^2 - 264S^3 - 455S^4 - 13S^5)/[24(1-S)^5]$$

$$A_{44} = (10S^3 - 174S^4 + 291S^5 + 278S^6)/[48(3+2S)(1-S)^5]$$

$$A_{51} = (-1184 + 32S + 1329S^2 + 21712S^3 + 20940S^4 + 12554S^5 - 500S^6 - 3341S^7 - 670S^8)$$
$$/[64\sinh(kD)(3+2S)(4+S)(1-S)^6]$$

$$A_{53} = (4S + 105S^2 + 198S^3 - 1376S^4 - 1302S^5 - 117S^6 + 58S^7)$$
$$/[32\sinh(kD)(3+2S)(1-S)^6]$$

$$A_{55} = (-64 + 272S^4 - 1552S^5 + 852S^6 + 2029S^7 + 430S^8)$$
$$/[64\sinh(kD)(3+2S)(4+S)(1-S)^6]$$

$$B_{11} = 1$$

$$B_{33} = \cosh(kD)(1+2S)/[2(1-S)]$$

$$B_{31} = -(1+3S+3S^2+2S^3)/[8(1-S)^3]$$

$$B_{33} = -B_{31}$$

$$B_{42} = \coth(kD)\left(6 - 26S - 182S^2 - 204S^3 - 25S^4 + 26S^5\right)/[6(3+2S)(1-S)^4]$$

$$B_{44} = \coth(kD)\left(24 + 92S + 122S^2 + 66S^3 + 67S^4 + 34S^5\right)/[24(3+2S)(1-S)^4]$$

$$B_{51} = -(B_{53} + B_{55})$$

$$B_{53} = 9(132 + 17S - 2216S^2 - 5897S^3 - 6292S^4 - 2687S^5 - 194S^6 + 467S^7 + 82S^8)$$
$$/[128(3+2S)(4+S)(1-S)^6]$$

$$B_{55} = 5(300 + 1579S + 3176S^2 + 2949S^3 + 1188S^4 + 675S^5 + 1326S^6 + 827S^7 + 130S^8)$$
$$/[384(3+2S)(4+S)(1-S)^6]$$

$$C_0 = \sqrt{\tanh(kD)}$$

$$C_2 = C_0(2 + 7S^2)/[4(1-S)^2]$$

$$C_4 = C_0(4 + 32S - 116S^2 - 400S^3 - 71S^4 + 146S^5)/[32(1-S)^5]$$